applied optics

Closure and uncertainty assessment for ocean color reflectance using measured volume scattering functions and reflective tube absorption coefficients with novel correction for scattering

Alberto Tonizzo,[1] Michael Twardowski,[2,*] Scott McLean,[3] Ken Voss,[4] Marlon Lewis,[5] and Charles Trees[6]

[1]GTF LLC, 30-77 31st St. #1, Astoria, New York 11102, USA
[2]Harbor Branch Oceanographic Institute, Florida Atlantic University, 5600 US 1 N, Ft. Pierce, Florida 34946, USA
[3]Ocean Networks Canada Innovation Centre, University of Victoria, 2300 McKenzie Avenue, Victoria, British Columbia V8W 2Y2, Canada
[4]Physics Department, University of Miami, Miami, Florida 33146, USA
[5]Department of Marine Science, Dalhousie, Halifax, Nova Scotia, Canada
[6]Centre for Marine Research and Exploration, La Spezia, Italy
*Corresponding author: mtwardowski@fau.edu

Received 6 September 2016; revised 23 November 2016; accepted 23 November 2016; posted 30 November 2016 (Doc. ID 274965); published 28 December 2016

Optical closure is assessed between measured and simulated remote-sensing reflectance (R_{rs}) using Hydrolight radiative transfer code for five data sets that included a broad range of both Case I and Case II water types. Model-input inherent optical properties (IOPs) were the absorption coefficient determined with a WET Labs ac9 and the volume scattering function (VSF) determined with a custom *in situ* device called MASCOT. Optimal matchups were observed using measured phase functions and reflective tube absorption measurements corrected using a scattering error independently derived from VSF measurements. Absolute bias (δ) for simulations compared to measured R_{rs} was 20% for the entire data set, and 17% if a relatively shallow station with optical patchiness was removed from the analysis. Approximately half of this δ is estimated to come from uncertainty in radiometric measurements of R_{rs}, with the other half arising from combined uncertainties in IOPs, radiative transfer modeling, and related assumptions. For exercises where such δ can be tolerated, IOPs have the potential to aid in ocean color validation. Overall, δ was roughly consistent with the sum of uncertainties derived from associated measurements, although larger deviations were observed in several cases. Applying Fournier–Forand phase functions derived from particulate backscattering ratios according to Mobley *et al.* [Appl. Opt. 41, 1035 (2002)] resulted in overall δ that was almost as good (23%) as simulations using measured phase functions. Possibilities for improving closure assessments in future studies are discussed.

OCIS codes: (010.0010) Atmospheric and oceanic optics; (010.4450) Oceanic optics; (280.0280) Remote sensing and sensors.

https://doi.org/10.1364/AO.56.000130

1. INTRODUCTION

Understanding how the different components of seawater alter the propagation of incident sunlight through scattering and absorption is essential to using remotely sensed ocean color observations effectively. This is particularly apropos in heterogeneous coastal waters, where the different optically significant components (phytoplankton, detrital material, inorganic minerals, etc.) vary widely in concentration, often independently from one another. Inherent optical properties (IOPs) such as absorption and the volume scattering function (VSF) form the link between these biogeochemical constituents of interest and the apparent optical properties (AOPs), which are dependent on the IOPs and the light field. Understanding this interrelationship is at the heart of successfully carrying out inversions of satellite-measured radiance to IOPs and ultimately to biogeochemical properties, while minimizing uncertainties for future satellite imaging missions. So-called closure analyses between measured AOPs and AOPs simulated from measured

IOPs and incident light conditions are necessary to evaluate inherent uncertainties in high-quality data sets before those data can be included in assessing uncertainties specific to AOP-IOP inversion algorithms.

Simulating AOPs such as remote-sensing reflectance from IOPs also has potential in validating ocean color satellite measurements if sufficient accuracy can be achieved. This was one of the concepts proposed as part of a NASA-supported effort called Spectral Ocean Radiance Transfer Investigation and Experiment (SORTIE) to assess and improve uncertainties associated with VC2 (vicarious calibration and characterization) of ocean color sensors [1]. SORTIE included the simulation of AOPs such as remote sensing reflectance from measured IOPs in spatial mapping exercises to evaluate ocean color subpixel and interpixel variability. While introducing several additional elements of uncertainty relative to direct radiometric measurements, an IOP-based approach has potential advantages that include avoiding wave focusing of light fields in surface waters, reliable and practical autonomous data collection, mapping capabilities with towed or flow-through systems, and a lessened requirement for synchronization with satellite overpass. In this context, the effort here extends previous SORTIE work to more rigorously evaluate uncertainties in simulating AOPs from IOPs and the potential for aiding validation of ocean color for future missions such as the NASA Plankton, Aerosol, Cloud, and ocean Ecosystem (PACE) imager with planned launch in 2022 (http://pace.gsfc.nasa.gov/).

Uncertainties inherent to data sets arise from the various IOP and radiometry measurements, assumptions about data gaps, space-time discrepancies, and any other assumptions used in radiative transfer equation (RTE) computations. Many of these sources of uncertainty are nontrivial. IOPs required to compute radiance fields are the VSF and absorption coefficient, along with inelastic effects such as Raman scatter that may be readily calculated (e.g., [2]). Since commercially available devices measuring the VSF with sufficient angular resolution have not been available, this important parameter has typically not been directly resolved in past closure assessments, requiring assumptions. Exceptions are the closure test included in Mobley *et al.* [3] and offshore and inshore sites assessed in Chang *et al.* [4]. Both studies used VSF measurements from a custom device called the MVSM [5] deployed at the LEO-15 site off the coast of New Jersey. Several other recent closure studies have used analytical phase functions from Fournier and Forand [6], including Mobley *et al.* [3], Bulgarelli *et al.* [5] at the Acqua Alta Oceanographic Tower (AAOT) site in the Adriatic Sea, Tzortziou *et al.* [7] in Chesapeake Bay, Maryland, U.S., Gallegos *et al.* [8] in lakes on the South Island of New Zealand, Lefering *et al.* [9] in the Ligurian Sea and west coast of Scotland, and Pitarch *et al.* [10] in north-Ionian and Adriatic waters.

For more than two decades, the only sensor for measuring in-water absorption coefficients spectrally with fine-scale depth resolution has been WET Labs ac devices, where absorption is resolved with a reflective tube methodology that requires a significant correction for scattered light not included in the measurement [11, 12–15]. The most widely applied correction methods for this large error have required nonideal assumptions, such as negligible absorption in the near-IR spectral domain [14], not supported in recent observations of natural samples [15–21].

Accuracy of in-water profiling radiometry measurements can be consistently better than 7% when following careful protocols [1,22,23], although important aspects of these protocols such as considerable repetition of vertical profiling to average the effects of wave focusing at the surface [24–26] are not always possible because of practical constraints on a ship.

When also considering typical space-time disparities in IOP and radiometry measurements, it is small wonder closure assessments, even in high-quality data sets in relatively simple aquatic regimes, often show poor agreement between measured and modeled reflectance (and are rarely reported). In cases where reasonable agreement is achieved, so many assumptions are required, often applied with varying degrees of subjectivity, that one is not sure how to gauge confidence in the result. Indeed, fully assessing uncertainties of simulations in the context of the component measurements, assumptions, and RTE modeling is almost impossible for many cases. For example, how would one estimate the uncertainty in using a VSF shape from Petzold collected in San Diego Harbor in 1972 [27] in reflectance simulations for any other time or place?

With recent technological advances in measuring in-water VSFs [28,29], as well as a newly developed and validated method to correct for the scattering error in WET Labs ac devices [13], there is now the opportunity to assess closure in ocean color validation data sets with fewer assumptions and better constrained uncertainties than previously possible. Five specific data sets collected during NASA ocean color work in 2007–2008 are considered for this assessment, where the scope of measurements, sensor characterization, and careful attention to protocols and accuracy render these data state-of-the-art. Sampling locations were south of Lanai, the Ligurian Sea, southern California coast off San Diego, and the New York bight. The overall objective is to assess uncertainties in current capabilities to simulate ocean color using state-of-the-art approaches and to try and reconcile those uncertainties with what we know of uncertainties associated with the individual components (i.e., sensor measurements, assumptions, and modeling). We can then assess the degree to which apparent closure in uncertainties is currently achievable, and whether there are sources of uncertainty still being missed.

2. METHODS

A. Data Sets

Table 1 provides a general description of the five field efforts included in the analysis. The Hawaii, Ligurian Sea, and coastal San Diego data sets were collected as part of the NASA SORTIE project. Stations are only considered here where the full suite of IOP and radiometry measurements were made under clear skies devoid of clouds. Because of the VC^2 nature of SORTIE, these locations were chosen for their low atmospheric aerosol optical thickness. The location south of Lanai was adjacent to the Marine Optics BuoY (MOBY) for ocean color calibration, and one of the stations in the Ligurian Sea was adjacent to the European BOUSSOLE ocean optics buoy (French acronym "BOUée pour l'acquiSition d'une Série Optique à Long termE", or "Buoy for the Acquisition of a Long-Term Optical Time

Table 1. Field Site Descriptions

Data Set	Dates	# Stations	Coordinates (min/max Lat *N* and Long *E*)	Radiometry System Used
New York bight (NYB1)	5/2007	7	40.2687/40.5 −74.16/−73.5961	Biospherical SubOps
New York bight (NYB2)	11/2007	6	40.3448/40.4468 −73.9152/−73.4498	Biospherical SubOps
South of Lanai, Hawaii (HI)	3/2007	4	21.2742/21.2769 −157.9205/−157.9135	Satlantic Hyperpro II
Ligurian Sea (LS)	9/2008	4	43.3844/43.8051 7.8845/10.0642	Satlantic Hyperpro II
San Diego coast (SD)	1/2008	3	32.733/32.933 −117.3667/−117.45	Satlantic Hyperpro II

Series" [30]). The Hawaii and coastal San Diego data sets may be considered Case I (cf. [31]), with the Ligurian Sea comprising a mix of Case I and Case II. Radiometry measurements were made with a hyperspectral Satlantic Hyperpro II with bandpass specifications characterized by the National Institute of Standards and Technology (NIST). We have used these data previously to assess inversion to IOPs [32], accuracy in radiometric measurements [1], and the bidirectional reflectance distribution function (BRDF) [33]. Stations included from the New York bight field efforts were collected under clear skies to skies with sparse cloud cover (less than 15%). Atmospheric aerosol loading is generally very high in this region. Radiometry measurements were collected using a 19-wavelength Biospherical Sub-Ops sensor by a NASA team led by *S*. Hooker. All data from this region are considered Case II.

Other than inelastic effects such as Raman scatter and fluorescence, the IOPs required to compute radiance fields are the VSF and absorption coefficient. Descriptions of field measurements and protocols are detailed below. All sensors were mounted in a custom cage with a 10 Hz SBE49 conductivity-temperature-depth sensor (SeaBird Electronics, Inc.), with data concurrently multiplexed and time-stamped with a WET Labs DH-4 into archives for later extraction, processing, and final merging. The instrument package was self-powered with submersible 31 A-h Sartek battery packs and self-recording with flash-card memory installed in the DH-4. Deployment protocols followed that described by Twardowski *et al.* [34] except where noted.

B. VSF Measurements

The VSF $\beta(\theta)$ [m^{-1} sr^{-1}] describes the angular distribution of scattered light from an incident unpolarized beam, defined as the radiant intensity $dI(\theta)$, scattered from a volume element dV, in a unit solid angle centered in direction θ, per unit irradiance E: $\beta(\theta) = (1/E)dI(\theta)/dV$ [35]. Assuming azimuthal symmetry and integrating the VSF over all solid angles (i.e., 0 to π rad) yields the total scattering coefficient, b [m^{-1}]. The phase function $\tilde{\beta}$ is the VSF normalized to total scattering, or $\beta(\theta)/b$ [sr^{-1}]. Integrating the VSF in the backward direction (i.e., $\pi/2$ to π rad) yields the backscattering coefficient, b_b [m^{-1}], of particular importance to remotely sensed water-leaving radiance. The backscattering ratio $\tilde{b}_b = b_b/b$ [unitless]. Subtracting the VSF contribution from pure seawater $\beta_w(\theta)$ [36] allows derivation of the particulate fractions for the parameters above, namely $\beta_p(\theta)$, b_p, $\tilde{\beta}_p(\theta)$, b_{bp}, and $\tilde{b}_{bp}$. Particulate backscattering is typically no more than 3% of particulate scattering in natural waters [37–40].

Few measurements of the full VSF in seawater have been made over the last several decades. Key obstacles have been (1) a single oceanic VSF typically has more than a 6 order of magnitude dynamic range in scattering intensity from near forward to backward angles; additionally, at any one angle, the magnitude of scattering can vary over 4 orders of magnitude in marine waters; (2) the magnitude of scattering is low in the backward direction, particularly with respect to stray light reflections within sampling chambers and contaminating ambient solar flux in subsurface waters; and (3) accurate calibration protocols have been lacking.

Here, the VSF was resolved with depth with the Multi-Angle Scattering Optical Tool (MASCOT), used previously in several studies on particle scattering and ocean color [29,41–48]. It uses a 30 mW 658 nm laser diode source (World Star Tech model TECRL-30G-658) and 17 independent silicon diode detectors spaced from 10° to 170° in 10° increments relative to the incident beam [29]. Sampling rate for all detectors is 20 Hz. The distance from the source and detector windows to the center of the sample volume is 10 cm. A wedge depolarizer installed in the source beam path provides unpolarized incident irradiance. Additional MASCOT details are described in [29], and calibration methodology is described in [29] and [38]. Estimated accuracy is 4% or better at all angles. In some cases, a detector malfunctioned, requiring interpolation (see Section 2.E.2).

A WET Labs ECO-BB3 measured the VSF in the backward direction using broad angular weighting functions centered at 124° and spectrally at 469, 530, and 657 nm. Deployment, calibration, data processing, and derivation of backscattering coefficients followed protocols described in [38].

C. Absorption and Attenuation Measurements

A WET Labs ac9 measured absorption (a_m) and attenuation (c_m) in seawater flowing through independent 25 cm path-length cells [34,49]. These parameters were used to derive absorption (a_{pg}) and attenuation (c_{pg}) by dissolved and particulate constituents in seawater as detailed below. For detailed definitions of these IOPs, refer to Mobley [35]. Spectral bands resolved for both a_{pg} and c_{pg} were centered at 412, 440, 488, 510, 532, 555, 650, 676, and 715 nm. The ac9 attenuation measurement is made with a 0.9° acceptance for scattered light. Purified water blank calibrations to quantify drift were carried out within 2 d of

in situ measurements. For cases when the ac9 was deployed horizontally, the blank measurements were made horizontally with the ac9 secured in its cage. Corrections for time lags (the time required for a sample to travel from the plumbing intake to measurement inside the flow cell), the temperature and salinity dependence of pure water absorption and attenuation [34,50], and drift were applied in postprocessing [34].

The absorption measurement uses a reflective quartz tube with a diffuser in front of a large area detector to collect most of the scattered light in the cell, but there is a residual scattering error ϵ (estimated at 10–30% of total scattering) requiring additional correction (i.e., removal via subtraction) [12,14,49]. Conventional protocols for correcting this spectral scattering error such as the so-called baseline (BL) and proportional (PROP) corrections described in Zaneveld *et al.* [14] require an assumption that all measured signal in the near-IR can be attributed entirely to ϵ (i.e., there is negligible actual absorption in the near-IR) (see Table 2 for details). Observations using a variety of different approaches have not supported this assumption [15–21], with Röttgers *et al.* [11] finding an average of 21.2% of absorption at 715 nm determined with an ac9 being "true" absorption for water in the Elbe river estuary and German Bight/Baltic Sea. Note ϵ is a function of the angular shape of the VSF and thus will vary with particle composition [15].

BL and PROP have been community standard methods in correcting ac9 absorption spectra for the last 20 years and were included for comparison. Additionally, scattering errors were derived independently with concurrent VSF measurements using a method based on modeled angular weighting functions for the scattering error presented in McKee *et al.* [15], evaluated in detail for ac devices in Stockley *et al.* [13]. The McKee *et al.* [15] weighting functions deviate from the theoretical weighting function of zero contribution from 0 to 41.7°, and 1 from 41.7 to 180°, with 41.7° being the angle of total internal reflection (TIR) for a quartz tube filled with water, surrounded by an air gap [14]. McKee *et al.* [15] simulated the effect of varying reflectivity efficiency (from 95 to 100%) of the flow tube wall and observed significant contribution to weightings at angles smaller than the angle of TIR. The amount of scattering in this angular range that is included increases dramatically with small decreases in the reflectivity of the flow tube surface from the ideal value of 100% originally assumed by Zaneveld *et al.* [14].

With $\beta(\theta)$ and an appropriate angular weighting function $W_\epsilon(\theta)$, ϵ may be derived by integrating with respect to angle,

$$\epsilon = 2\pi \int_0^\pi \sin(\theta) W_\epsilon(\theta) \beta(\theta) \mathrm{d}\theta. \quad (1)$$

Based on the results of [13], $W_\epsilon(\theta)$ computed by [15] for reflectivities of 97% and 98% were found to be most representative of flow tubes for WET Labs ac devices. The ϵ parameter derived with a reflectivity of 98% was chosen for the corrections herein (also see Section 4, Discussion). Since the VSF is resolved at 658 nm, $\epsilon(658)$ was extrapolated to the other ac9 wavelengths using the PROP method (VSF98P) described in [14], where $\epsilon(658)/b(658)$ is held spectrally constant. Values of $b(658)$ were derived from $c_m(650) - a_m(650)$ measurements, assuming a flat b spectrum from 650 to 658 nm. After all corrections, total particulate scattering b_p was derived from $c_{pg} - a_{pg}$. Scattering corrections are summarized in Table 2.

Figure 1 shows spectral corrections to absorption for three representative stations. Station NYB2-009 demonstrates a case with significant real absorption at 715 nm associated with VSF98P, about 50% of $a_m(715)$. For all data sets, VSF98P $a_{pg}(715)$ averaged 29% of $a_m(715)$. For NYB1, NYB2, and SD data sets, $c_m - a_m$ did not exhibit significant spectral dependency, so BL and PROP tended to be very similar. Small spectral decreases in $c_m - a_m$ of ~10% and ~20% from the blue to red were observed for LS and HI data sets, respectively. For the Hawaii data (see station HI-007), the VSF98P correction was slightly higher (~0.003 m^{-1}) than $a_m(650)$, so resultant absorption values were slightly negative. These were set equal to zero for simulations. More significant negative values at 715 nm were likely due to uncertainty in temperature-salinity corrections applied to $a_m(715)$, where the observed −0.009 m^{-1} value would equate to a ~3°C discrepancy if just a function of temperature. Note such bias at 715 nm also would affect BL and PROP, highlighting potentially significant issues with bias in using near-IR absorption in scattering correction algorithms, especially in clear waters.

Table 2. Descriptions of Scattering Error Corrections Applied for WET Labs ac Device Absorption Measurements[a]

Label	Description	Formula for Scattering Error, $\epsilon(\lambda)$
BL	Measured absorption at 715 nm reference wavelength assumed to be 100% scattering error (i.e., assumes no real absorption in the near-R). Error assumed spectrally constant.	$a_m(715)$
PROP	Measured absorption at 715 nm reference wavelength assumed to be 100% scattering error. Error is scaled spectrally by the ratio of measured total scattering ($c - a$) (i.e., assuming that the ratio of scattering error to total scattering is constant spectrally).	$a_m(715)\frac{c_m(\lambda)-a_m(\lambda)}{c_m(715)-a_m(715)}$
VSF98P	Scattering error is independently derived by convolving measured VSF β with angular weighting function W_ϵ of the scattering error for WET Labs ac device reflective tube modeled in McKee *et al.* [15]. Weighting function associated with 98% tube reflectivity is applied after Stockley *et al.* [13]. Error is scaled spectrally according to the PROP method.	$2\pi \int_0^\pi \sin(\theta) W_\epsilon(\theta) \beta(\theta, 658) \mathrm{d}\theta \frac{c_m(\lambda)-a_m(\lambda)}{c_m(650)-a_m(650)}$

[a]Scattering errors are subtracted from measured absorption a_m.

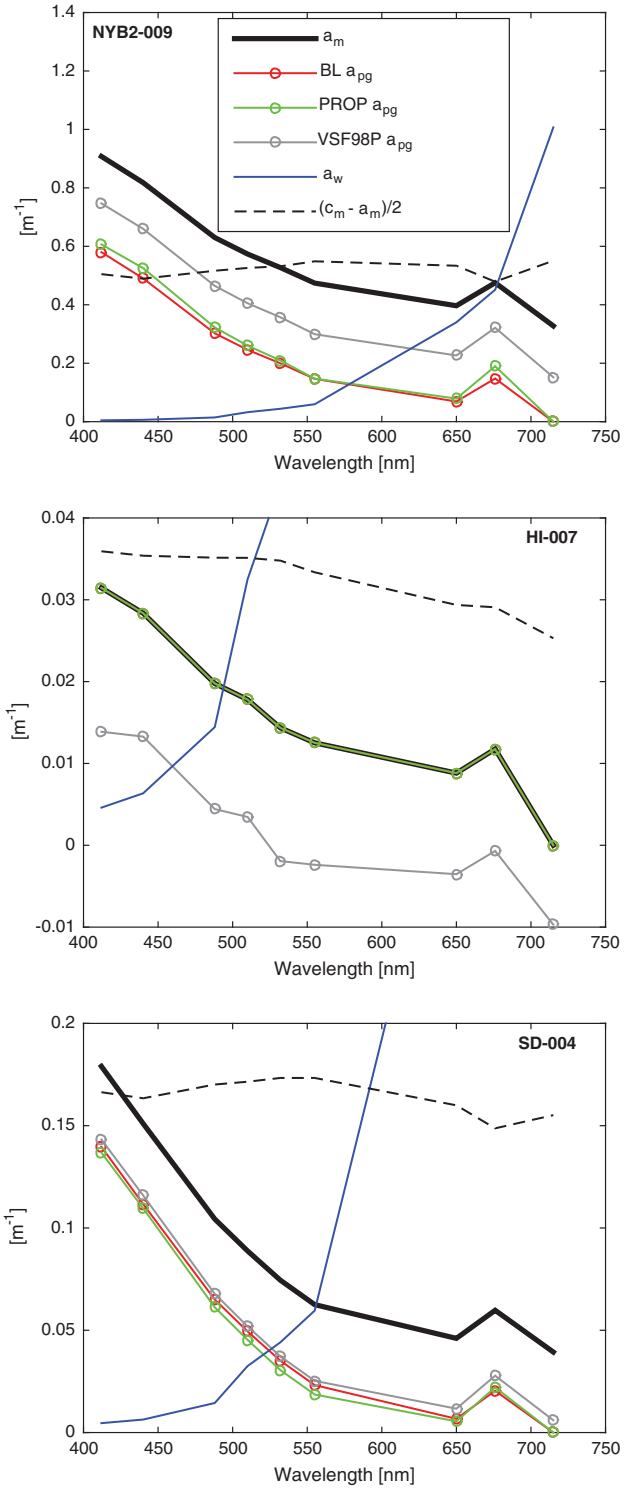

Fig. 1. Measured and corrected IOP spectra for selected stations, highlighting differences among scattering corrections used in this study. Note these stations correspond, from top to bottom, to stations in Figs. 4B, 4C, and 4E, respectively. IOPs are 1 m averages of data collected at the surface of each cast.

With purified water calibrations exhibiting good replicability, absolute uncertainty in c_{pg} and a_{pg} uncorrected for scattering error is estimated at ≤ 0.004 m^{-1} (~0.002 m^{-1} in waters with low attenuation), which is primarily a bias error, as random electronic noise is ≤ 0.001 m^{-1} at all wavelengths. Because of the relatively small sample volume (~30 mL), additional variability in the signal is observed due to patchiness in the larger size domain of particle fields [51], which can be reduced by averaging (i.e., effectively increasing the sample volume). The scattering error correction employing the VSF as described above is expected to have an accuracy of $\leq 2\%$ in coastal waters [13]. Derived b_p has a propagated uncertainty of ≤ 0.0056 m^{-1} with an additional ~2% accuracy from the scattering correction to absorption. As a constraint on ac9 absorption measurement error, an attempt was made to use radiometry measurements (see next section) to approximate absorption based on Gershun's Equation, with some assumptions about the equivalence of various diffuse attenuation coefficients [52]. However, profile data were generally noisy due to surface wave focusing, resulting in larger uncertainties for derived absorption relative to *in situ* measurements.

D. Radiometry Measurements

Radiometry and IOP data were collected at the same locations within 10–15 min on average, and sometimes concurrently.

For the New York bight data sets, upwelling nadir radiance and downwelling irradiance were resolved at 19 wavelengths through the water column with a Biospherical Sub-Ops radiometer (next generation currently sold commercially as C-Ops) customized to have a small form factor and slow vertical descent rate [53]. Protocols for operation, deployment, and data processing are described in [54].

For HI, LS, and SD data sets, hyperspectral upwelling nadir radiance and downwelling irradiance profiles through the water column were measured with custom, stray-light corrected Satlantic HyperPro II hyperspectral radiometers. In-air surface irradiance (E_s) reference measurements were obtained from a HyperOCR hyperspectral irradiance sensor. The HyperPro II had 138 surface irradiance channels, 138 downwelling irradiance channels, and 138 upwelling radiance channels between 350 and 800 nm. For SORTIE, all 255 channels from 300–1100 nm were reported for stray-light corrections, but only channels from 350–900 nm were processed to radiometric units. The HyperPro II also used optical shutters for dark readings during deployment. Variable and adaptive integration times were used for all spectrometers [1].

For the SORTIE campaigns, the multicast ensemble method was used [24–26]. Derived radiometric products (Level 4 data) were K_d and K_u for all wavelengths, surface optical data (E_d and L_u propagated to surface level), water leaving radiances, L_w, L_{wn}, surface remote-sensing reflectances (R_{rs}), and Q factor if surface E_u and L_u were available. Surface products represent the propagation of radiances/irradiances to a theoretical depth just below the surface [55,56]. R_{rs} was then calculated by propagating radiances through the surface using Fresnel reflectances and normalizing by the above-water downwelling irradiances for each band [1,22].

Voss *et al.* [1] reported a 7% averaged difference for deployed radiance sensors and a <2% averaged difference for deployed irradiance sensors when compared with NIST values, which gives a propagated uncertainty of < ~7.3% for R_{rs}. Zibordi *et al.* [24] also estimated an additional 1.2%

uncertainty for the derivation of L_w from casts of L_u. The combined uncertainty is thus estimated at ~8.5%.

E. Radiative Transfer Simulations

1. Hydrolight Input

Hydrolight (HL) version 5.2.2 was used to solve the RTE in assessments of optical closure between measured and simulated optical properties. Typical vertical profiles of total absorption and total VSF data cannot be directly ingested by HL. The option in the HL User Interface "Measured IOPs" was used to input IOPs, which assumes data consistent with that of WET Labs ac devices (i.e., absorption and attenuation data without pure seawater contributions), which are separate inputs. Pure water absorption was taken from [57]. Scattering of pure seawater at the measured temperature and salinity for each station was obtained using the values derived by [36].

Two protocols for data input for HL were followed (Fig. 2), one that used the built-in derivation of the Fournier–Forand (FF) phase function from $\tilde{b}_{bp}$ based on [3], and one that used the measured phase function (MPF). The former is consistent with typical simulations from recent literature (e.g., [10,9,7]) and is an excellent approximation for particulate phase functions in natural waters across the entire angular range. For each set of simulations, the BL, PROP, and VSF98P methods of correcting scattering in a_{pg} from the ac9 were tested.

For FF simulations, additional required inputs were spectral c_{pg}, obtained from the ac9, and spectral b_{bp}. The latter was computed by first deriving $b_{bp}(658)$ from integrating MASCOT measurements over the backward direction, dividing by $b_p(658)$ (see Section 2.E.2) to obtain $\tilde{b}_{bp}(658)$, and then multiplying by spectral b_p, with the assumption that $\tilde{b}_{bp}$ was spectrally independent. This assumption was verified with $\tilde{b}_{bp}$, derived using ancillary backscattering data from the three-wavelength ECO-BB3 scattering sensor and ac9-derived b. Backscattering data from MASCOT were used in the simulations because of higher accuracy. HL uses the spectral c_{pg} and a_{pg} inputs to compute spectral b_p, computes $\tilde{b}_{bp}$ from the spectral b_{bp} input and this spectral b_p, and subsequently derives a FF phase function from $\tilde{b}_{bp}$ according to [3]. HL then multiplies the phase function by spectral b_p to obtain the spectral VSF in the RT calculations. This is carried out at every depth. There was no attempt to correct c_{pg} (or derived b_p) for acceptance angle issues, as, in practice, the value of c_{pg} has little effect on such simulations because of the compensating role in deriving both $\tilde{b}_{bp}$ (and subsequent FF phase function) and b_p [9]. This HL protocol is considered optimal for ac9 data collected in concert with spectral backscattering.

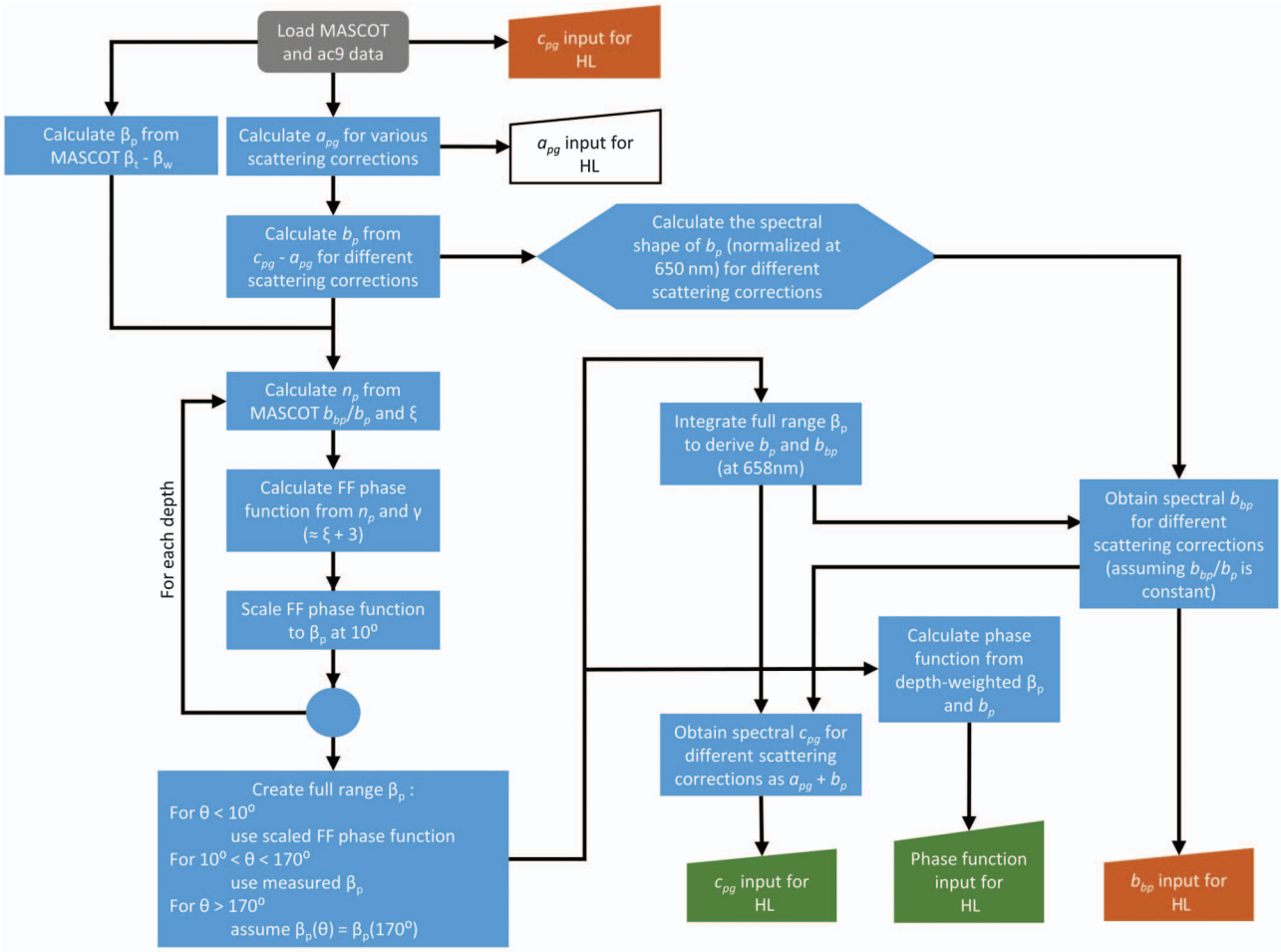

Fig. 2. Summary flow chart of preparation of IOPs for HL input. Orange HL input boxes correspond to FF phase function protocol; green HL input boxes correspond to protocol with measured VSFs; the white input box is common to both paths of data input. See text for details.

When using measured VSFs as input to HL, the VSF over the full angular range 0–180° is required, which must be divided by VSF-integrated scattering to convert to a phase function, and then discretized to the coordinate system employed by HL (see Section 2.E.2). HL only accepts one input for the phase function for a simulation, so depth profiles of the VSF must first be depth-weighted according to the contribution to water-leaving radiance. This was carried out following the model of Zaneveld *et al.* [58]. Additional inputs were spectral c_{pg} and spectral a_{pg}. Values of c_{pg} for these simulations cannot be taken from an ac9, since derived spectral b_p would not match the integrated scattering of the full VSF because of the ac9 acceptance angle error in the c measurement. As a result, spectral c_{pg} was computed from adding VSF-integrated scattering to spectral a_{pg}. VSF-integrated scattering was spectrally scaled from $b_p(658)$, according to the spectral shape of $c_{pg} - a_{pg}$ from the ac9.

Wind speed was taken from field notes for each station. Solar zenith angle was calculated by HL based on location and time of the day. The default values of the atmospheric parameters were used by RADTRANX in HL to compute the solar and sky spectral irradiance incident onto the sea surface from the measured total (sun + sky) irradiance. The percentage of cloud cover was also entered based on the field notes for each station (nominally zero).

Raman scattering was included in the simulations, while fluorescence (both by dissolved organic material (DOM) and chlorophyll) was neglected. Output bands were centered at the ac9 wavelengths 412, 440, 488, 510, 532, 555, and 650, with bandwidth of 10 nm. Wavelength 676 nm was not included due to the confounding effects of chlorophyll fluorescence. Wavelength 715 nm was also not considered, since this spectral region is characterized by very high water absorption (>1 m^{-1}) and near zero R_{RS}, where bias errors become dominant. Near-IR R_{RS} can be useful in turbid waters with high particle backscattering; such waters were not sampled here. Several intermediate bands were also added in the simulations, ranging from 407 to 720 nm, separated by no more than 10 nm. These bands are useful for obtaining reasonable IOP resolution for the inelastic scatter calculations [59].

2. Preparing Measured Phase Functions for Hydrolight

Since HL computes radiances propagating into finite solid angles known as quads [60], the depth-weighted particulate phase function $\tilde{\beta}_p$ obtained from MASCOT must be discretized. The latest HL discretization routine [59] constructs a lookup table of phase function values with resolution of 0.1°, so MASCOT data was extrapolated and interpolated over the full range of 0° to 180° with this resolution.

FF analytical phase functions ([6,61] latest version in [62]) were computed for every depth to provide an approximation of the VSF shape in the angular range 0° to 10°, a region lacking MASCOT data. Inputs for the phase function model of bulk refractive index (n) and particle size distribution slope (γ) were derived from the backscattering ratio and spectral slope (ξ) of c_p data using the algorithm of [37]. The resulting phase function in the 0° to 10° region was then scaled to match MASCOT β_p at 10°. Other shapes for the near-forward VSF were tried and had negligible effect on reflectance simulations, consistent with findings by others (e.g., [10,9,63]), since small-angle scattering does not significantly change the shape of the upwelled light field at the surface. Different shapes have a dramatic effect on integrated scattering, however, which is why MASCOT-specific b_p values were used in deriving parameters for the simulations. For angles greater than 170°, $\beta_p(170°)$ was extrapolated as a constant. Since the solar zenith was never near 0°, this angular region of the phase function was not critical in the simulations. This region also has a negligible effect on the b_{bp} integration due to the $2\pi \sin(\theta)$ weighting. Final interpolation to 0.1° resolution was carried out with a Piecewise Cubic Hermite Interpolating Polynomial (pchip in MATLAB) on log-log transformed data.

3. RESULTS

Table 3 shows selected IOPs for all stations sampled.

Differences between MPFs and derived FF phase functions are shown in Fig. 3. In the backward direction, agreement was better than 20% for most stations and averaged near 0%.

A. Representative Cases

Simulated and measured R_{rs} are compared in Fig. 4 for a representative station from each data set. Results for different scattering corrections for absorption and modeled FF versus MPFs are shown. Depth-weighted [58] $\langle b_b/(a+b_b)\rangle$ (not shown) were also computed and showed close agreement in spectral shape with simulated R_{rs}. Spectral shapes were generally consistent for various simulations for an individual station.

Moreover, simulation results using BL- and PROP-corrected absorption were similar in all cases, since $c_m - a_m$ was relatively flat spectrally. Results using VSF98P were significantly different from BL and PROP results in many cases, usually when VSF98P predicted significant absorption in the red and near-IR. The exception was the HI data, where VSFP98 exhibited lower absorption (and higher R_{rs}).

For station NYB2-009, both absorption correction and phase function had dramatic effects on simulation results. The simulation using VSF98P was significantly lower than results from BL and PROP due to higher absorption in the red and near-IR. Simulations using MPFs were ~25% higher than those using FF phase functions, with VSF98P-MPF showing closest agreement overall.

For the clear HI-007 station, greatest differences were observed in the blue. Differences in low particulate absorption toward the red were insignificant in HI simulation results because of the dominance of pure water absorption. Moreover, HI results were weakly dependent on phase function, with FF and MPF agreeing within a few percent throughout the backward. VSF98P appeared to overcorrect absorption in the blue (resulting in higher simulated R_{rs}), whereas BL and PROP appeared to undercorrect. The latter may be due to residual bias in the temperature-salinity correction at $a_m(715)$ (also see Fig. 1).

LS-086 simulations showed underestimation in the blue (as did simulations for all LS stations), with MPFs exhibiting higher simulated R_{rs} than simulations with FF. Simulations from SD-004 showed a strong dependence on phase function, with ~40% difference in results between FF and MPF inputs. Simulations for SD again underestimated R_{rs} in the blue.

Table 3. IOP Parameters from All Stations: Depth-Weighted a_{pg}, b_{bp}, and c_{pg} for Selected Wavelengths and Mixed Layer Depth (MLD) when Present[a]

	$\langle a_{pg}\rangle$[m^{-1}]			$\langle b_{bp}\rangle$[10^{-3} m^{-1}]			$\langle c_{pg}\rangle$[m^{-1}]		
Station	488 nm	532 nm	650 nm	488 nm	532 nm	650 nm	650 nm	$\langle\tilde{b}_{bp}\rangle$	MLD [m]±1 m
NYB1-001	0.517	0.299	0.110	25.7	26.4	26.4	2.741	0.010	5
NYB1-006	0.673	0.425	0.211	22.9	25.1	24.5	2.334	0.011	6
NYB1-007	0.155	0.081	0.025	9.6	9.4	8.1	1.398	0.006	10
NYB1-008	0.596	0.367	0.142	40.3	41.3	40.8	2.338	0.018	N/A
NYB1-013	0.572	0.362	0.139	47.7	47.6	45.3	2.306	0.020	7
NYB1-014	0.078	0.037	0.008	5.8	5.6	4.5	0.879	0.005	N/A
NYB1-017	0.562	0.336	0.125	37.6	37.8	37.1	2.237	0.017	N/A
NYB2-008	0.245	0.169	0.088	6.7	6.8	7.0	3.000	0.002	N/A
NYB2-009	0.458	0.345	0.223	17.2	18.2	18.1	2.682	0.007	N/A
NYB2-031	0.222	0.161	0.074	6.4	6.0	6.2	0.948	0.006	N/A
NYB2-034	0.343	0.258	0.138	8.6	9.0	9.4	1.649	0.007	N/A
NYB2-035	0.450	0.320	0.186	10.1	10.2	10.4	1.652	0.007	N/A
NYB2-039	0.298	0.203	0.102	9.7	9.8	9.8	1.266	0.007	8
HI-003	0.007	0.002	~0	1.1	1.1	0.9	0.064	0.013	N/A
HI-004	0.005	~0	~0	1.3	1.2	1.0	0.064	0.013	N/A
HI-007	0.004	~0	~0	1.3	1.2	1.0	0.064	0.013	N/A
HI-008	0.005	~0	~0	1.3	1.2	1.0	0.064	0.013	N/A
LS-027	0.021	0.010	~0	1.1	1.1	1.0	0.165	0.007	N/A
LS-045	0.022	0.010	~0	0.9	0.9	0.8	0.149	0.007	12
LS-086	0.021	0.012	~0	1.6	1.6	1.3	0.725	0.002	N/A
LS-087	0.052	0.036	0.020	6.1	5.8	5.1	0.373	0.014	7
SD-000	0.042	0.010	~0	2.6	2.6	2.2	0.560	0.004	N/A
SD-004	0.071	0.040	0.013	3.1	3.2	2.8	0.624	0.004	12
SD-007	0.066	0.035	0.007	2.4	2.4	2.1	0.664	0.004	12

[a]Scattering correction VSF98P was used to correct ac9 absorption. See text for derivation of backscattering values.

B. Closure Assessments for All Data

Performance metrics included the coefficient of determination for the fitted regression line (R^2),

$$R^2 = 1 - \frac{\sum_{i=1}^{n}(y_i - \hat{y}_i)^2}{\sum_{i=1}^{n}(y_i - \bar{y})^2}, \tag{2}$$

where n is the number of data points (seven bands, as 676 and 715 are excluded, for each of the 24 stations), y is the measured R_{rs}, $\bar{y}$ is the mean of the measured R_{rs} values, and $\hat{y}$ are the R_{rs} values predicted by HL simulations. R^2 is a statistical measure of the proportion of the variance in the dependent variable that is predictable from the independent variable given a particular model. It is not necessarily a good metric for agreement between simulated and measured data, since small variance may be observed around a regression model that significantly deviates from a 1:1 relationship.

Percent δ, absolute and relative, are also commonly used metrics

$$\%\delta = 100 * \frac{\delta}{\bar{y}}, \qquad \delta = \frac{\sum_{i=1}^{n}|y_i - \hat{y}_i|}{n}, \tag{3}$$

$$\%\delta_{\text{rel}} = 100 * \frac{\delta_{\text{rel}}}{\bar{y}}, \qquad \delta_{\text{rel}} = \frac{\sum_{i=1}^{n}(y_i - \hat{y}_i)}{n}. \tag{4}$$

If δ_{rel} is near zero, the match-up regression will be near 1:1, but this provides no indication of magnitude of residuals. The δ metric, also known as mean absolute error, takes into account the absolute magnitude of the residuals, giving them equal weight. Finally, percent root mean square error (%RMSE), is a measure of accuracy and potential forecasting errors in simulating R_{rs} when the errors may be assumed to be unbiased and normally distributed [64]

$$\%\text{RMSE} = 100 * \frac{\text{RMSE}}{\bar{y}}, \qquad \text{RMSE} = \sqrt{\frac{\sum_{i=1}^{n}(y_i - \hat{y}_i)^2}{n}}. \tag{5}$$

RMSE gives greater weight to larger errors than δ. Since bias errors are expected to be more significant than random,

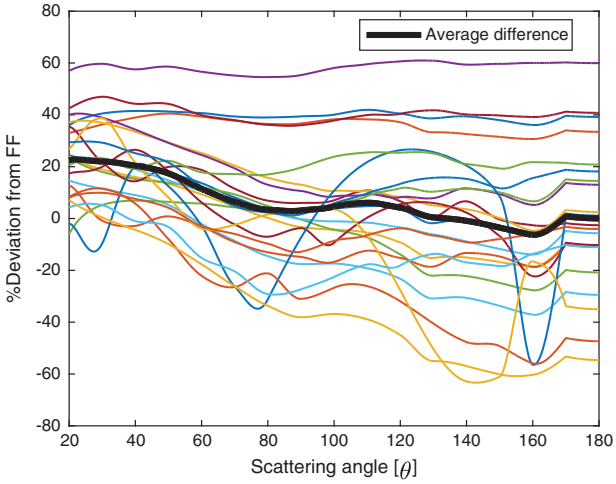

Fig. 3. Percent difference between FF phase functions and phase functions derived from measured VSFs.

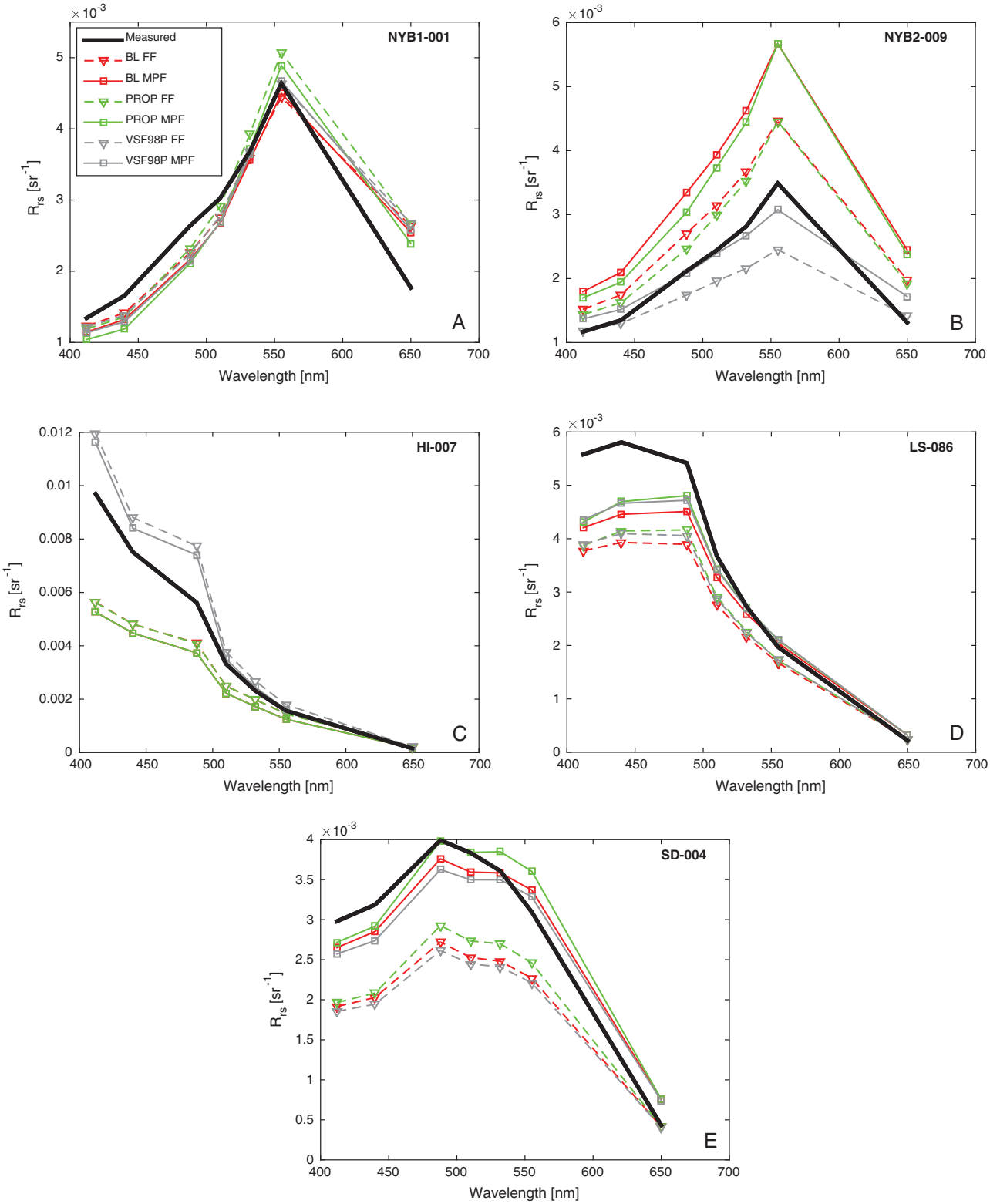

Fig. 4. Modeled and measured R_{rs} for representative cases for the five datasets included in this study: (A) NYB1-001, (B) NYB2-009, (C) HI-007, (D) LS-086, and (E) SD-004. R_{rs} measurements were interpolated to ac9 wavelengths (see text).

normally distributed errors, (1) $\%\delta$ is expected to be the most appropriate metric to assess simulation matchups, and (2) Type I linear regression slopes are considered rough approximations.

Closure was assessed between simulated and measured R_{rs} for all 24 stations (Figs. 5 and 6), with statistical results in Table 4. BL, PROP, and VSF98P correction methods for

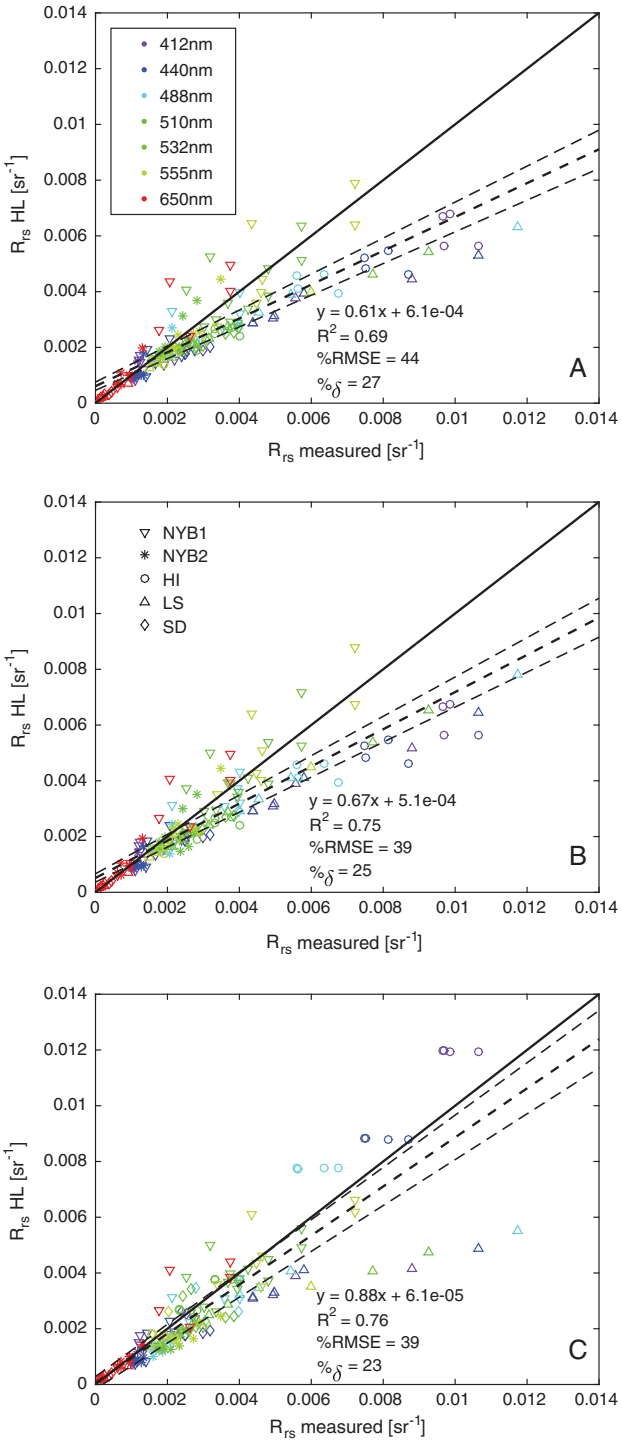

Fig. 5. Comparison between modeled and measured R_{rs} corresponding to absorption corrected using (A) the BL method, (B) the PROP method, and (C) the VSF98P method. A FF phase function was used, derived from $\tilde{b}_{bp}$ in HL. Legend for symbols is in (B). Solid line shows the 1:1 relationship, while dashed lines show the linear regression fit with standard error bounds. $N = 168$ for all plots.

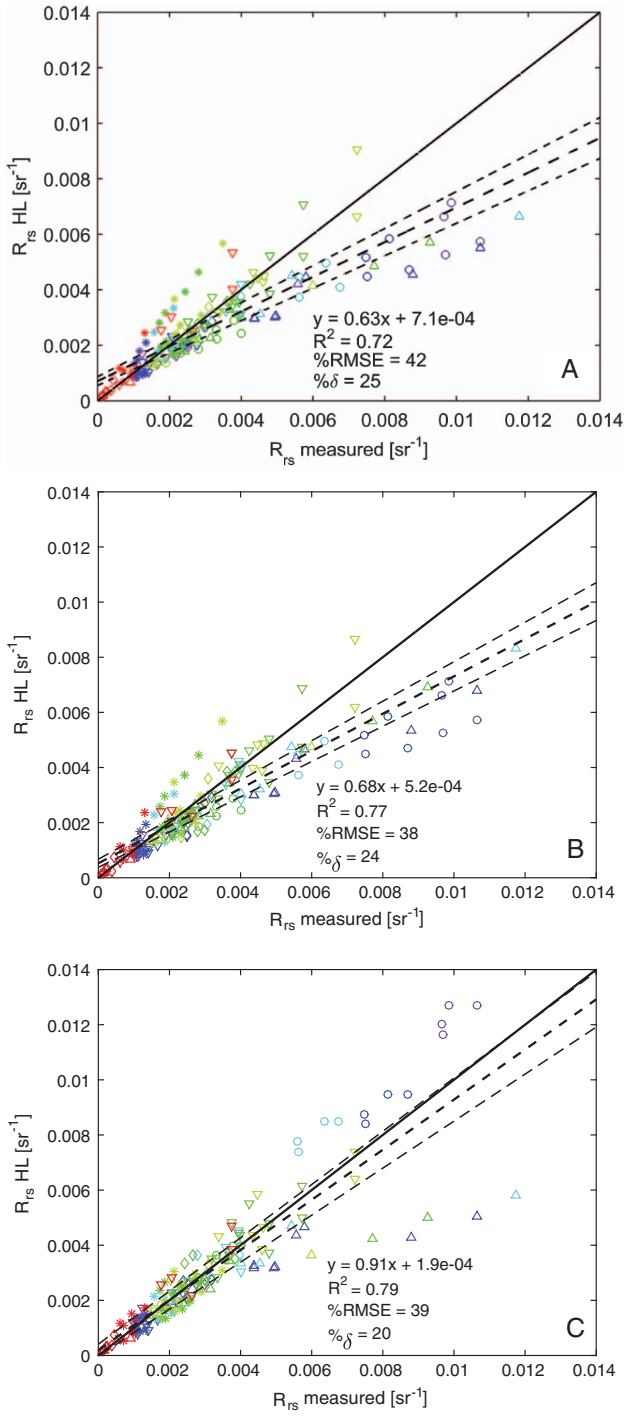

Fig. 6. Same as in Fig. 5 except measured VSF (MPF) was used as input in HL.

absorption were tested for FF (Fig. 5) and MPFs (Fig. 6). VSF98P-MPF simulations (Fig. 6C) typically showed the lowest %δ, although results with FF input were never more than a few percent worse. Results from applying the BL and the PROP absorption corrections generally agreed within a few percent. BL and PROP usually underestimated R_{rs}, resulting from overcorrection of the scattering error for absorption due to the null $a_{pg}(715)$ assumption. As expected from comparisons of ac device absorption with a bench-top integrating cavity device [13], the VSF98P absorption correction consistently resulted in the best overall agreement metrics between simulated and measured R_{rs}. This agreement provides an additional, independent

Table 4. Statistics Comparing R_{RS} Simulations to Measurements for Different Scenarios

		BL-FF	BL-MPF	PROP-FF	PROP-MPF	VSF98P-FF	VSF98P-MPF
Slope	Overall	0.61	0.63	0.67	0.68	0.88	0.91
	NYB1	0.91	1.33	1.03	1.27	0.87	1.00
	NYB2	1.08	0.93	0.96	0.87	0.63	0.80
	HI	0.58	0.60	0.58	0.60	1.19	1.24
	LS	0.51	0.54	0.63	0.67	0.44	0.47
	SD	0.64	0.91	0.70	0.92	0.62	0.88
R^2	Overall	0.69	0.73	0.75	0.78	0.76	0.79
	NYB1	0.69	0.86	0.76	0.87	0.79	0.87
	NYB2	0.76	0.54	0.65	0.58	0.43	0.64
	HI	0.64	0.62	0.64	0.62	0.89	0.86
	LS	0.49	0.56	0.67	0.73	0.40	0.46
	SD	0.51	0.90	0.58	0.63	0.34	0.80
%RMSE	Overall	43	41	39	38	39	39
	NYB1	27	19	24	18	23	18
	NYB2	20	43	23	40	30	24
	HI	109	121	109	121	65	73
	LS	129	120	103	93	139	132
	SD	46	19	38	36	48	27
$\%\delta(\%\delta_{rel})$	Overall	27 (19)	24 (14)	25 (16)	24 (14)	23 (10)	20 (3)
	NYB1	23 (1)	14 (2)	19 (2)	14 (4)	19 (0)	14 (−1)
	NYB2	13 (0)	29 (−18)	17 (5)	20 (−10)	25 (24)	21 (1)
	HI	31 (31)	32 (32)	31 (31)	32 (32)	17 (−17)	16 (−16)
	LS	33 (33)	29 (29)	29 (29)	25 (25)	31 (31)	28 (27)
	SD	26 (26)	11 (8)	21 (21)	20 (16)	27 (13)	15 (−5)

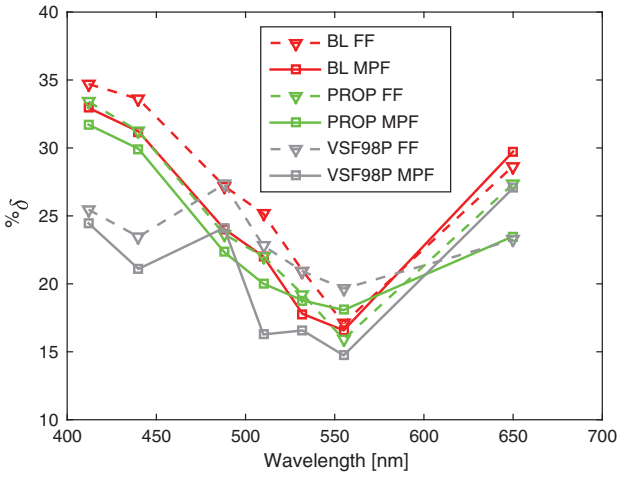

Fig. 7. Spectral δ for R_{rs} matchups, all data.

form of validation to the conclusion of optimal correction method found by [13].

Figure 7 shows spectral $\%\delta$ for simulations from 412 to 650 nm. The VSF98P-MPF correction consistently performed as well or better for most wavelengths. MPFs also performed as well or better than FF, although results were always similar.

Plots of measured and simulated spectral R_{rs} for VSF98P-MPF are shown for all 24 stations in Fig. 8. In general, agreement in the blue was generally better for more turbid stations, whereas agreement in the red was best for clearer waters, where pure water absorption dominated. Overestimation in the red was common for more turbid stations.

4. DISCUSSION

A. Bootstrapping Errors

When the inputs of a model have well-defined uncertainties, a local sensitivity analysis can be performed. Multiple simulations are run with varying inputs around original values within known uncertainty ranges. In our case, the inputs to vary are the measured a_{pg} and VSF.

All data were varied by constant amounts as an estimate of the influence of input uncertainties on errors in final simulated R_{rs}. Adjustments of +0.002 and +0.005 m^{-1} were made to a_{pg} at every wavelength, at every depth for the VSF98P-MPF simulations. The primary sources of bias error for the ac9 (e.g., calibration drift, internal temperature corrections, suboptimal cleanliness for optical windows) generally do not scale with magnitude [34]. Offsets of 0.002 m^{-1} are at the level of expected precision considering the calibration protocols that were followed, but a 0.005 m^{-1} bias offset could be realistic after applying scattering corrections to absorption. Negative offsets were not considered, because these resulted in negative a_{pg} values in several cases. Adjusting all a_{pg} data by +0.002 m^{-1} resulted in δ for R_{rs} of 6.3% in the blue, decreasing to <1% in the red, relative to the VSF98P-MPF simulations (Table 5). Higher errors in the blue were driven by clear HI and LS data sets with low natural a_{pg} and a_w values, so uncertainties were significant relative to magnitude. Error δ jumped to 14.2% in the blue for a +0.005 m^{-1} adjustment in a_{pg}. Uncertainty in a_{pg} had a negligible effect in the red, where water absorption was dominant. Absolute error in R_{rs} for all 24 stations, including all wavelengths, was 3.3% with a +0.002 m^{-1} adjustment in a_{pg} and 7.8% with a +0.005 m^{-1} adjustment.

The largest source of uncertainty for MASCOT VSFs is the scaling factor derived in calibration, which is multiplicative, although errors from dark offsets can become nonnegligible in very clear waters. Scaling factors of ±2% and ±5% were applied to the readings of all the MASCOT VSFs at every depth for VSF98P-MPF simulations. Deviations greater than 5% are not expected based on the protocols followed. Resulting δ in R_{rs} for the entire data set after a +2% adjustment in the VSF was 1.1% in the blue increasing to 2.3% in the red, relative to the VSF98P-MPF simulations (Table 5). For the +5% adjustment to the VSF, δ in R_{rs} was 3.0% in the blue, increasing to 5.8% in the red. Errors from adjusting the VSF by −2% and −5% were within 0.1% of errors observed for the positive adjustments. The clear water stations from HI and LS all had $\delta < 1\%$ at all wavelengths for the +2% adjustment, driving δ down for the entire data set, because of the significant contribution of pure seawater scattering in total scattering. For these clear stations, estimated uncertainties associated with dark offsets approached the 5% level, so that R_{rs} at 650 nm may be expected to have an additional ∼6% associated error. Absolute errors in simulated R_{rs} for all data were 1.9% and 4.7%, with adjustments in the VSF of +2% and +5%, respectively.

No adjustment in a_{pg} or VSF for all data was able to improve the absolute error of 20% obtained for the overall matchups between VSF98P-MPF simulation results and measured R_{rs}. In individual cases, adjusting input IOPs within uncertainty ranges improved spectral agreement for matchups, but not in all cases (Fig. 9). Simulations from the Hawaii data were sensitive to small changes in absorption in the blue because of very low values of both a_{pg} and a_w, so approximate agreement could be observed with +0.002 to +0.005 m^{-1} shifts in

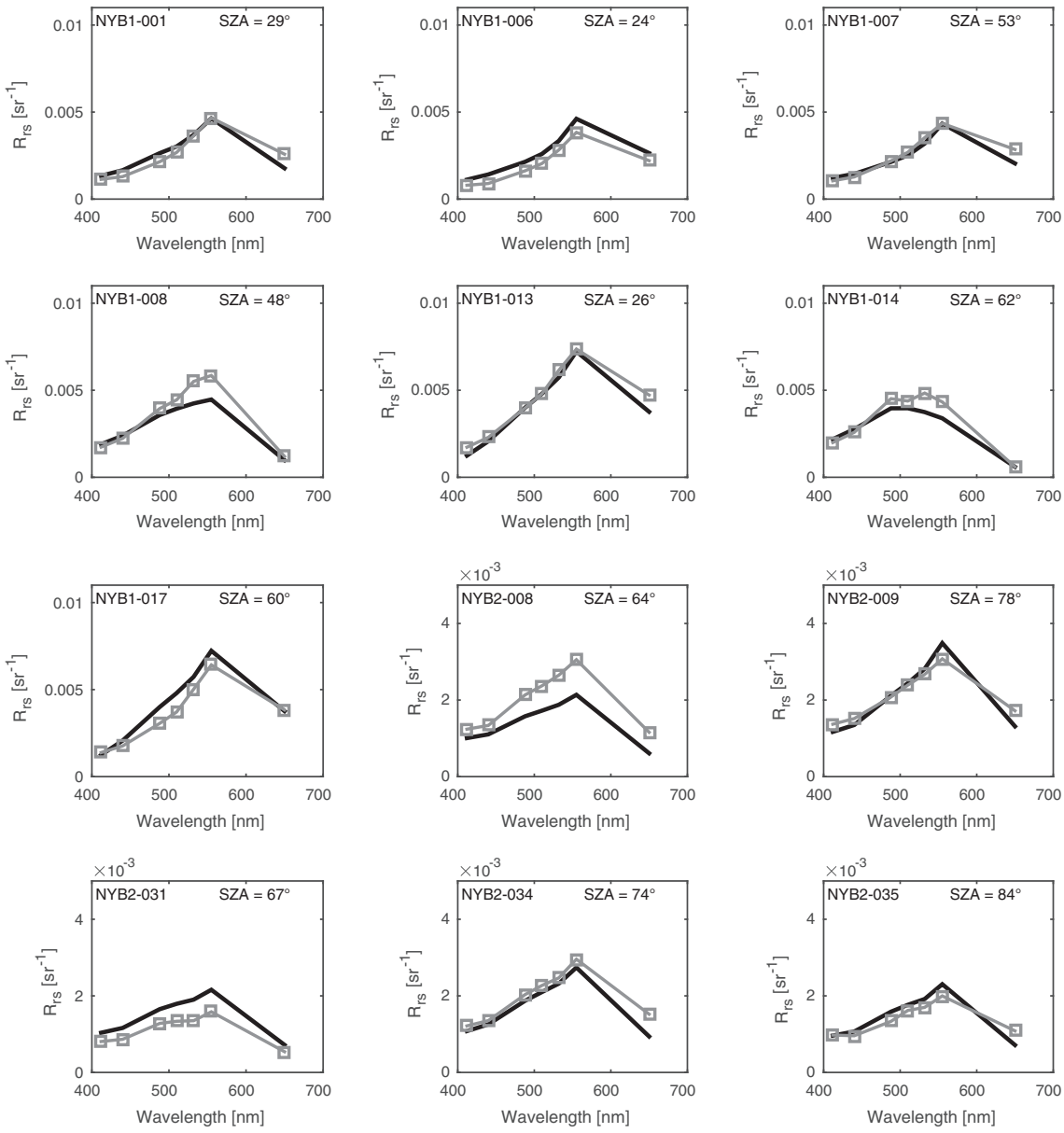

Fig. 8. (Continued)

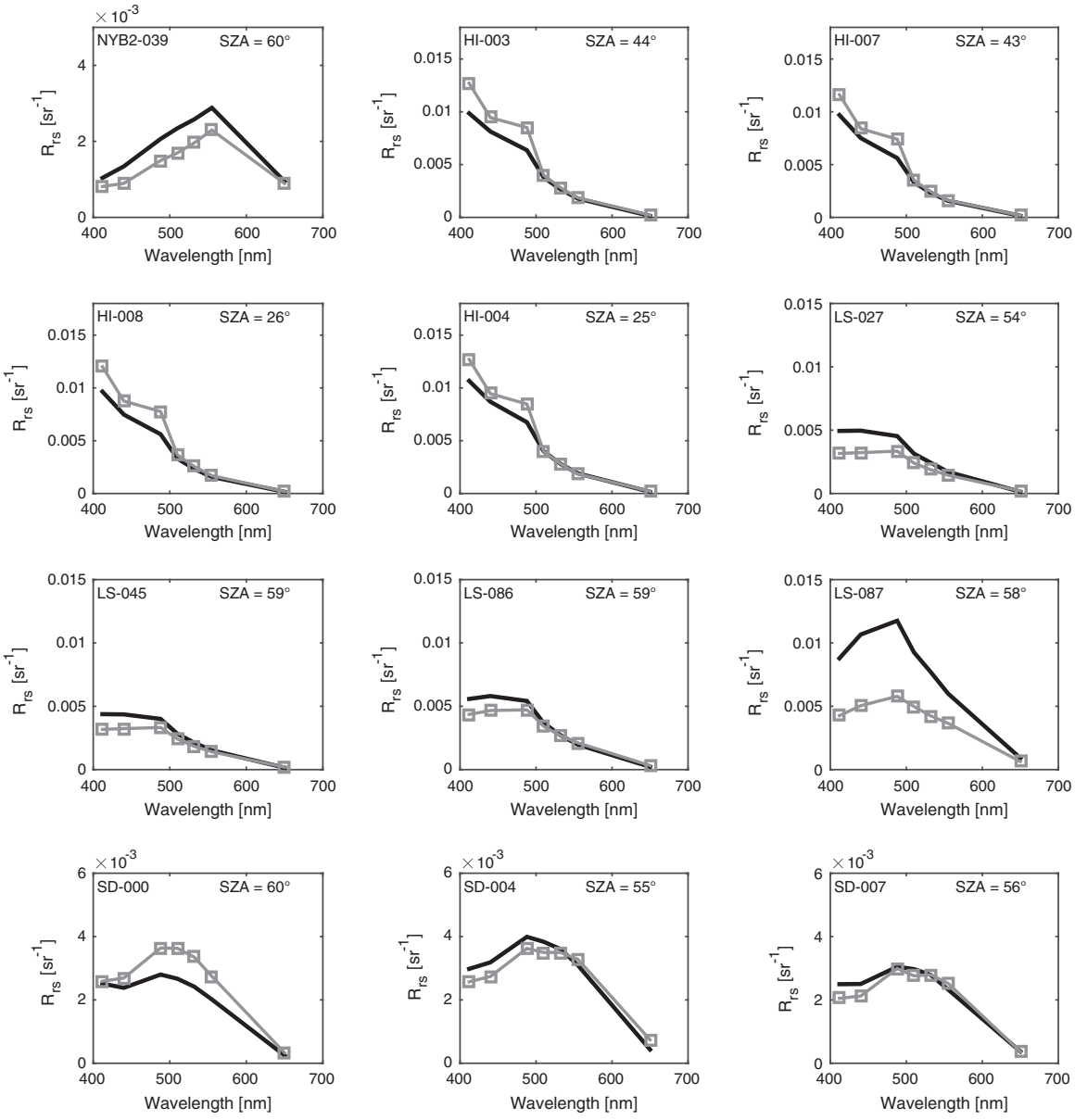

Fig. 8. R_{rs} measured (thick black line) and simulated (gray line, empty squares) for the best performing simulation scenario (i.e., VSF98P-MPF).

Table 5. Absolute Error %δ in R_{rs} after Bootstrapping Uncertainties in a_{pg} and the VSF for All 24 Stations

	a_{pg}		VSF	
$\lambda(nm)$	$+0.002$ m^{-1}	$+0.005$ m^{-1}	$+2\%$	$+5\%$
412	6.3%	14.2%	1.1%	3.0%
440	5.4%	12.5%	1.4%	3.7%
488	4.4%	10.8%	1.7%	4.3%
510	2.8%	7.0%	1.9%	4.9%
532	1.9%	4.8%	2.0%	5.3%
555	1.6%	3.9%	2.2%	5.6%
650	0.6%	1.4%	2.3%	5.8%
overall	3.3%	7.8%	1.9%	4.7%

absorption (Fig. 9A). However, no combination of adjusted absorption and VSF within reasonable ranges could provide suitable matchups in the blue for the Ligurian Sea data (Fig. 9B), suggesting other significant form(s) of δ must be responsible.

B. Uncertainty Budget

The pertinent assessment of uncertainty for simulation results is absolute δ, as residual errors in R_{rs} are dominated by bias errors in the measurements and model assumptions (i.e., they are not expected to be normally distributed). Overall, we obtained a δ of 20% for the VSF98P-MPF simulation results for all data, or 17% if station LS-087 is removed (see below).

The preceding analysis leads to the rough generalization that a ± 0.002 m^{-1} uncertainty in a_{pg} corresponds to δ in simulated R_{rs} of ~4% for our diverse data set, reaching as high as ~8% in the blue for clear waters, and likely higher for even clearer

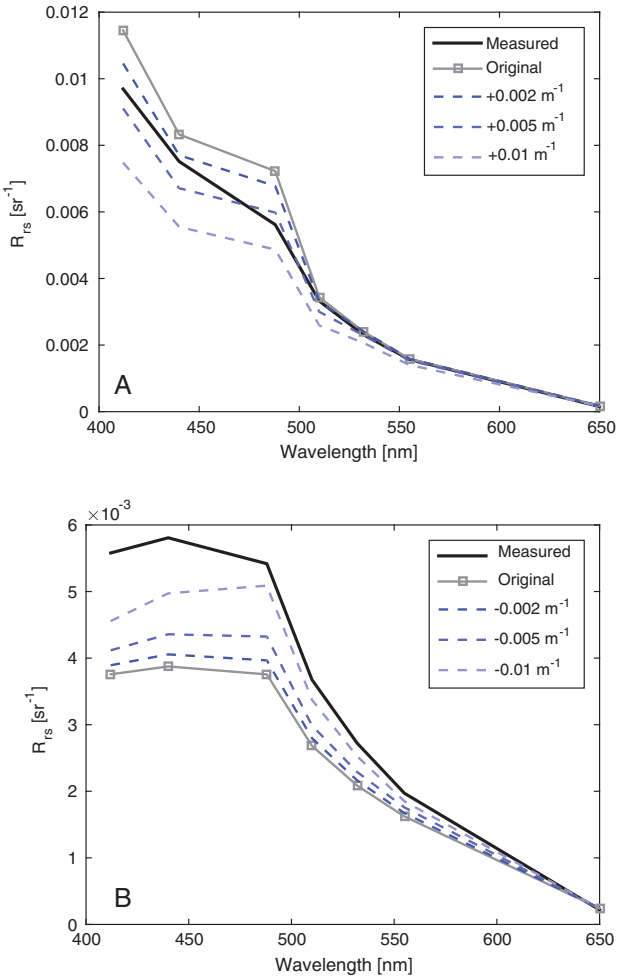

Fig. 9. Bootstrapping uncertainties in a_{pg} for (A) HI-007 and (B) LS-086. Negative values indicate uncertainties were subtracted from a_{pg}.

waters such as the South Pacific gyre. For the VSF, a ±2% uncertainty resulted in δ of ~2% for the entire data set, but may be as high as ~7% in very clear waters where dark offset uncertainty can become significant. Thus, for the entire data set, aggregate uncertainties in a_{pg} and VSF are expected to contribute ~6% in absolute error, and up to ~15% in the blue for very clear waters. This is based on best possible uncertainties in IOP measurements. Accuracies in derived R_{rs} from radiometry measurements for the range 400–650 nm are expected to be ≤ 8.5% (see Section 2.D). Summing IOP-derived and radiometry-derived uncertainties therefore yields ~15% and, by generalization, may represent the theoretical expectation for the accuracy of closure studies across both Case I and II waters with similar methods. In very clear waters, up to 25% may be expected in the blue, even with state-of-the-art methods. These estimates are in line with our estimations of overall uncertainty from δ in the data sets, although this assumes the worst case (i.e., all biases are additive, none compensative). This assessment also does not consider estimated uncertainties in pure water absorption of ~0.0005 m^{-1} in the blue to ~0.003 m^{-1} at 650 nm [57].

As mentioned, bootstrapping within known uncertainty ranges for a_{pg} and the VSF did not bring simulated R_{rs} within expected uncertainties of measured R_{rs} (≤ 20%) in some cases. Notable examples are (1) substantial underestimation through the blue and green for station LS-087 (see matchup panel in Fig. 8), (2) consistent underestimation in the blue for all Ligurian Sea data (Figs. 8,9B), and (3) overestimation in the mid-visible despite reasonable agreement in the blue and red for stations NYB1-008, NYB1-014, NYB2-008, and SD-000 (Fig. 8).

Station LS-087 was unique in being relatively shallow (13 m bottom depth, but still slightly deeper than $1/K_d$ at all wavelengths) with spatial heterogeneity in optical properties noted during measurements. Varying optical properties between IOP and radiometry measurements is therefore likely, and influence from bottom reflectance may have affected the radiometry casts. Removing this single station from the analysis reduces overall δ in the VSF98P-MPF simulations from 20% to 17%.

Several other sources of δ error are possible that are difficult to quantify at this time. From an environmental perspective, these may include (1) breakup of particle aggregates from high shear in ac9 flow tubes (e.g., [65]), skewing particle size distributions to smaller particles and increasing absorption and scattering cross sections, (2) "randomization" of any naturally occurring preferential particle orientation [66,67], removing any directional dependencies in the IOPs and radiative transfer modeling, (3) variability in IOPs where measurements are lacking in the near-surface (shallower than ~0.5 m, including the surface skin), (4) ephemeral bubble populations near-surface [29,42,44], and (5) internal waves [68]. Additionally, even with the breadth of IOP measurements made, an assumption was still needed on the spectral consistency of phase function shape.

Other possible sources of δ relate to assumptions used in radiative transfer modeling with HL, including approximations of skylight versus direct, a single-phase function input for all depths, choosing to ignore fluorescence from DOM, and polarization effects. The latter is likely most significant, causing up to 20% errors in some simulations [59,69]. Simulation results typically matched measured R_{rs} more consistently in our data sets under cloudy skies, where polarization effects would be expected to be suppressed (data not shown). For comparison, preliminary radiative transfer simulations including full polarization were carried out by Dr. Bingqiang Sun (Texas A&M) using a 3D Monte Carlo model developed by Zhai *et al.* [69], with IOP data from station NYB1-001 as input. In some cases, substantially higher R_{rs} was obtained in the blue – more than 40% at 440 nm – for the fully polarized model, with an overall closer match to measured R_{rs}. This is a strong indication that polarization should be explicitly considered in future radiative transfer simulations and closure assessments.

Considering the challenges listed above, reasonable closure was achieved, comparable to previous studies using measured VSFs and/or independently corrected ac9 absorption. Chang *et al.* [4] reported spectral δ for R_{rs} ranging between 11% and 32% using absorption data from an ac9 and phase function measurements from a prototype VSF meter (MVSM; [28]) off coastal New Jersey. Tzortziou *et al.* [7] obtained excellent closure with δ [recomputed from original data according to

Eq. (3)], varying from 6.6% to 9.4% spectrally (412 to 670 nm) for water-leaving radiance L_w in Chesapeake Bay using FF phase functions and ac9 absorption data corrected for near-IR absorption from independent laboratory measurements. Gallegos *et al.* [8] obtained agreement in L_w comparable to that reported by Tzortziou *et al.* [7] for four lakes in New Zealand, also after correcting ac9 absorption based on lab measurements. As L_w lacks the downwelling irradiance normalization of R_{rs}, it may be expected to have lower overall uncertainties. These studies also did not sample very clear water, where IOP uncertainties can significantly influence simulation results.

Other studies assessing closure using ac9 data and FF phase functions include Bulgarelli *et al.* [5], Lefering *et al.* [9], and Pitarch *et al.* [10]. Bulgarelli *et al.* found relative bias $\%\delta_{\text{rel}}$ in individual simulation matchups as high as 50% in water column profiles of irradiance reflectance R (i.e., the ratio of upwelling irradiance to downwelling irradiance), although most matchups agreed within 20%. Lefering *et al.* [9] found % RMSE for their Ligurian Sea and west coast of Scotland data between 24% and 33% for subsurface R_{rs}, comparable to our results. They also found generally small influence from applying different scattering corrections to ac9 absorption data, consistent with results here obtained with BL and PROP. Finally, Pitarch *et al.* assessed closure matchups for 58 stations in Ionian and Adriatic waters using several possible scattering corrections for absorption, with $\%\delta_{\text{rel}} < 25\%$ at all wavelengths. All the above studies used HL for simulating radiometric parameters.

5. SUMMARY

Closure assessments are essential in characterizing inherent uncertainties before data sets can be used to assess performance of ocean color remote-sensing algorithms. Optical closure was assessed between measured and simulated R_{rs} using HL radiative transfer code for five data sets that included a broad range of both Case I and Case II water types. Optimal matchups were observed using measured phase functions and reflective tube absorption measurements corrected using a scattering error independently derived from VSF measurements. Absolute error δ for simulations compared to measured R_{rs} was 20% for the entire data set, and 17% if the shallow LS-087 station is removed from the analysis. This is about twice the δ observed in direct radiometric comparisons carried out by Voss *et al.* [1]. Overall, δ was roughly consistent with the sum of uncertainties derived from varying the input IOP measurements, although larger deviations were observed in several cases. Applying FF phase functions derived from b_{bp}/b_p according to Mobley *et al.* [3] resulted in an overall δ that was almost as good (23%) as results from simulations using MPFs when using the independently derived scattering correction for absorption.

There are several possibilities for improving closure assessments in future studies. With respect to radiative transfer modeling, full polarization should be considered, and the phase function should be allowed to vary with depth. On the experimental side, the high sensitivity of simulated R_{rs} on absorption, especially in clear Case I waters in the blue, is notable. Adjusting absorption spectra within expected measurement uncertainties of $+0.002$ and $+0.005$ m^{-1}, resulted in errors up to 10% and 20%, respectively, in R_{rs} matchups in the blue (Fig. 9A). From a measurement perspective, achieving 0.002 to 0.005 m^{-1} uncertainty levels in absorption is currently state-of-the-art, especially for *in situ* instrumentation. Nonetheless, this remains the largest source of δ in closure assessments in Case I water. Improved methodologies for increasing accuracy in absorption, preferably in undisturbed sample volumes, could have benefit in future algorithm development and validation. Finally, the assumption of a spectrally independent phase function could be avoided with direct *in situ* measurements of the VSF spectrally.

Funding. National Aeronautics and Space Administration (NASA); Office of Naval Research (ONR); Harbor Branch Oceanographic Institute Foundation.

Acknowledgment. Scott Freeman was instrumental in the collection of IOP field data, and Davide D'Alimonte assisted in the collection of radiometry data in the NYB. Dennis Clark and the MOBY Science Team are gratefully acknowledged for accommodating our participation on a MOBY operations cruise. Curt Mobley provided substantial assistance and discussion in the use of HL in analysis. Discussions with David McKee were also helpful in using HL. We are grateful to Bingqiang Sun and George Kattawar for simulating reflectance with Monte Carlo RT code with full polarization to compare with HL. Maria Tzortziou kindly provided data from Tzortziou *et al.* [7], Table 4. We are grateful to Jaime Pitarch, Grace Chang, Emmanuel Boss, and an anonymous reviewer for detailed reviews that substantially improved this paper. The crews of the R/V Alliance, R/V Connecticut, R/V Ka'imikai-O-Kanaloa, and R/V Klaus Wyrtki are acknowledged for their assistance in the field. Support for A.T. was provided by the Harbor Branch Oceanographic Institute Foundation through an award to M.T.

REFERENCES

1. K. J. Voss, S. McLean, M. Lewis, C. Johnson, S. Flora, M. Feinholz, M. Yarbrough, C. Trees, M. Twardowski, and D. Clark, "An example crossover experiment for testing new vicarious calibration techniques for satellite ocean color radiometry," J. Atmos. Ocean. Technol. **27**, 1747–1759 (2010).
2. T. K. Westberry, Z. Lee, and E. S. Boss, "Influence of Raman scattering on ocean color inversion models," Appl. Opt. **52**, 5552–5561 (2013).
3. C. D. Mobley, L. K. Sundman, and E. Boss, "Phase function effects on oceanic light fields," Appl. Opt. **41**, 1035–1050 (2002).
4. G. C. Chang, T. D. Dickey, C. D. Mobley, E. Boss, and W. S. Pegau, "Toward closure of upwelling radiance in coastal waters," Appl. Opt. **42**, 1574–1582 (2003).
5. B. Bulgarelli, G. Zibordi, and J. F. Berthon, "Measured and modeled radiometric quantities in coastal waters: toward a closure," Appl. Opt. **42**, 5365–5381 (2003).
6. G. R. Fournier and J. L. Forand, "Analytic phase function for ocean water," Proc. SPIE **2258**, 194–201 (1994).
7. M. Tzortziou, J. Herman, C. Gallegos, P. Neale, A. Subramaniam, L. Harding, and Z. Ahmad, "Bio-optics of the Chesapeake Bay from measurements and radiative transfer closure," Estuarine, Coastal Shelf Sci. **68**, 348–362 (2006).
8. C. L. Gallegos, R. J. Davies-Colley, and M. Gall, "Optical closure in lakes with contrasting extremes of reflectance," Limnol. Oceanogr. **53**, 2021–2034 (2008).

9. I. Lefering, F. Bengil, C. Trees, R. Röttgers, D. Bowers, A. Nimmo-Smith, J. Schwarz, and D. McKee, "Optical closure in marine waters from in situ inherent optical property measurements," Opt. Express **24**, 14036–14052 (2016).
10. J. Pitarch, G. Volpe, S. Colella, R. Santoleri, and V. Brando, "Absorption correction and phase function shape effects on the closure of apparent optical properties," Appl. Opt. **55**, 8618–8636 (2016).
11. R. Röttgers, D. McKee, and S. B. Woźniak, "Evaluation of scatter corrections for ac-9 absorption measurements in coastal waters," Methods Oceanogr. **7**, 21–39 (2013).
12. J. T. O. Kirk, "Monte Carlo modeling of the performance of a reflective tube absorption meter," Appl. Opt. **31**, 6463–6468 (1992).
13. N. Stockley, R. Röttgers, D. McKee, J. Sullivan, and M. Twardowski are preparing a manuscript to be called "Absorption measurements from an in-water reflective tube absorption meter: assessing uncertainties for different scattering correction algorithms," Opt. Express.
14. J. R. V. Zaneveld, J. C. Kitchen, and C. M. Moore, "The scattering error correction of reflecting-tube absorption meters," Proc. SPIE **2258**, 44–55 (1994).
15. D. McKee, J. Piskozub, R. Röttgers, and R. A. Reynolds, "Evaluation and improvement of an iterative scattering correction scheme for in situ absorption and attenuation measurements," J. Atmos. Ocean. Technol. **30**, 1527–1541 (2013).
16. R. Röttgers and S. Gehnke, "Measurement of light absorption by aquatic particles: improvement of the quantitative filter technique by use of an integrating sphere approach," Appl. Opt. **51**, 1336–1351 (2012).
17. S. Tassan and G. M. Ferrari, "An alternative approach to absorption measurements of aquatic particles retained on filters," Limnol. Oceanogr. **40**, 1358–1368 (1995).
18. S. Tassan and G. M. Ferrari, "A sensitivity analysis of the 'transmittance-reflectance' method for measuring light absorption by aquatic particles," J. Plankton Res. **24**, 757–774 (1998).
19. S. Tassan and G. M. Ferrari, "Variability of light absorption by aquatic particles in the near infrared spectral region," Appl. Opt. **42**, 4802–4810 (2003).
20. D. Stramski, M. Babin, and S. B. Woźniak, "Variations in the optical properties of terrigeneous mineral-rich particulate matter suspended in seawater," Limnol. Oceanogr. **52**, 2418–2433 (2007).
21. D. Stramski, S. B. Woźniak, and P. J. Flatau, "Optical properties of Asian mineral dust suspended in seawater," Limnol. Oceanogr. **49**, 749–755 (2004).
22. S. Hooker, S. McLean, J. Sherman, M. Small, G. Lazin, G. Zibordi, and J. Brown, "The seventh SeaWiFS intercalibration round-robin experiment (SIRREX-7), March 1999," (2002).
23. G. Zibordi, K. Ruddick, I. Ansko, G. Moore, S. Kratzer, J. Icely, and A. Reinart, "In situ determination of the remote sensing reflectance: an inter-comparison," Ocean Sci. **8**, 567–586 (2012).
24. G. Zibordi, F. Mélin, S. B. Hooker, D. D'Alimonte, and B. Holben, "An autonomous above-water system for the validation of ocean color radiance data," IEEE Trans. Geosci. Remote Sens. **42**, 401–415 (2004).
25. G. Zibordi, J. F. Berthon, F. Melin, and D. D'Alimonte, "Cross-site consistent in situ measurements for satellite ocean color applications: the BiOMaP radiometric dataset," Remote Sens. Environ. **115**, 2104–2115 (2011).
26. D. D'Alimonte, E. B. Shybanov, G. Zibordi, and T. Kajiyama, "Regression of in-water radiometric profile data," Opt. Express **21**, 27707–27733 (2013).
27. T. J. Petzold, *Volume Scattering Function for Selected Ocean Waters* (Scripps Institute of Oceanography, 1972).
28. M. E. Lee and M. R. Lewis, "A new method for the measurement of the optical volume scattering function in the upper ocean," J. Atmos. Ocean. Technol. **20**, 563–571 (2003).
29. M. Twardowski, X. Zhang, S. Vagle, J. Sullivan, S. Freeman, H. Czerski, Y. You, L. Bi, and G. Kattawar, "The optical volume scattering function in a surf zone inverted to derive sediment and bubble particle subpopulations," J. Geophys. Res. **117**, C00H17 (2012).
30. D. Antoine, P. Guevel, J. F. Deste, G. Becu, F. Louis, A. J. Scott, and P. Bardey, "The 'BOUSSOLE' buoy—a new transparent-to-swell taut mooring dedicated to marine optics: design, tests, and performance at sea," J. Atmos. Ocean. Technol. **25**, 968–989 (2008).
31. H. R. Gordon and A. Y. Morel, *Remote Assessment of Ocean Color for Interpretation of Satellite Visible Imagery: A Review* (Springer-Verlag, 1983).
32. H. R. Gordon, M. R. Lewis, S. D. McLean, M. S. Twardowski, S. A. Freeman, K. J. Voss, and G. C. Boynton, "Spectra of particulate backscattering in natural waters," Opt. Express **17**, 16192–16208 (2009).
33. A. Gleason, K. J. Voss, H. R. Gordon, M. Twardowski, J. Sullivan, C. Trees, A. Weidemann, J.-F. Berthon, D. Clark, and Z. Lee, "Detailed validation of the bidirectional effects in various case I and case II waters," Opt. Express **20**, 7630–7645 (2012).
34. M. S. Twardowski, J. M. Sullivan, P. L. Donaghay, and J. R. V. Zaneveld, "Microscale quantification of the absorption by dissolved and particulate material in coastal waters with an ac-9," J. Atmos. Ocean. Technol. **16**, 691–707 (1999).
35. C. D. Mobley, *Light and Water: Radiative Transfer in Natural Waters* (Academic, 1994), p. 592.
36. X. Zhang, L. Hu, and M.-X. He, "Scattering by pure seawater: effect of salinity," Opt. Express **17**, 5698–5710 (2009).
37. M. S. Twardowski, E. Boss, J. B. Macdonald, S. Pegau, A. H. Barnard, and J. R. V. Zaneveld, "A model for estimating bulk refractive index from the optical backscattering ratio and the implications for understanding particle composition in case I and case II waters," J. Geophys. Res. **106**, 14129–14142 (2001).
38. J. M. Sullivan, M. S. Twardowski, J. R. V. Zaneveld, and C. M. Moore, "Measuring optical backscattering in water," in *Light Scattering Reviews 7* (Springer, 2013).
39. E. Boss, S. Pegau, M. Lee, M. S. Twardowski, E. Shybanov, G. Korotaev, and F. Baratange, "The particulate backscattering ratio at LEO 15 and its use to study particles composition and distribution," J. Geophys. Res. **109**, C01014 (2004).
40. J. Sullivan, M. S. Twardowski, P. L. Donaghay, and S. Freeman, "Using scattering characteristics to discriminate particle types in US coastal waters," Appl. Opt. **44**, 1667–1680 (2005).
41. P. Brady, A. Gilerson, G. Kattawar, J. Sullivan, M. Twardowski, H. M. Dierssen, M. Gao, K. Travis, R. I. Etheredge, A. Tonizzo, A. I. Ibrahim, C. Carrizo, Y. Gu, B. J. Russell, K. Mislinski, S. Zhao, and M. E. Cummings, "Open-ocean fish reveal an omnidirectional solution to camouflage in polarized environments," Science **350**, 965–969 (2015).
42. H. Czerski, M. Twardowski, X. Zhang, and S. Vagle, "Resolving size distributions of bubbles with radii less than 30 μm with optical and acoustical methods," J. Geophys. Res. **116**, C00H11 (2011).
43. A. Gilerson, J. Stepinski, A. I. Ibrahim, Y. You, J. M. Sullivan, M. S. Twardowski, H. M. Dierssen, B. Russell, M. E. Cummings, P. Brady, S. A. Ahmed, and G. W. Kattawar, "Benthic effects on the polarization of light in shallow waters," Appl. Opt. **52**, 8685–8705 (2013).
44. K. Randolph, H. M. Dierssen, M. S. Twardowski, A. Cifuentes-Lorenzen, and C. J. Zappa, "Optical measurements of small deeply penetrating bubble populations generated by breaking waves in the southern ocean," J. Geophys. Res. Oceans **119** (2013).
45. J. Sullivan and M. Twardowski, "Angular shape of the volume scattering function in the backward direction," Appl. Opt. **48**, 6811–6819 (2009).
46. A. Tonizzo, J. Zhou, A. Gilerson, M. Twardowski, D. Gray, R. Arnone, B. Gross, F. Moshary, and S. Ahmed, "Polarization measurements in coastal waters: hyperspectral and multiangular analysis," Opt. Express **17**, 5666–5683 (2009).
47. Y. You, A. Tonizzo, A. Gilerson, M. E. Cummings, P. Brady, J. M. Sullivan, M. S. Twardowski, H. M. Dierssen, S. A. Ahmed, and G. W. Kattawar, "Measurements and simulations of polarization states of underwater light in clear oceanic waters," Opt. Express **50**, 4873–4893 (2011).
48. Y. Gu, C. Carrizo, A. A. Gilerson, P. C. Brady, M. E. Cummings, M. S. Twardowski, J. M. Sullivan, A. I. Ibrahim, and G. W. Kattawar, "Polarimetric imaging and retrieval of target polarization characteristics in underwater environment," Appl. Opt. **55**, 626–637 (2016).
49. J. R. V. Zaneveld, R. Bartz, and J. C. Kitchen, "A reflective-tube absorption meter," Proc. SPIE **1302**, 124–136 (1990).
50. W. S. Pegau, D. Gray, and J. R. V. Zaneveld, "Absorption and attenuation of visible and near-infrared light in water: dependence on temperature and salinity," Appl. Opt. **36**, 6035–6046 (1997).

51. N. T. Briggs, W. H. Slade, E. Boss, and M. J. Perry, "Method for estimating mean particle size from high-frequency fluctuations in beam attenuation or scattering measurements," Appl. Opt. **52**, 6710–6725 (2013).
52. J. R. V. Zaneveld, M. S. Twardowski, M. R. Lewis, and A. H. Barnard, "Radiative transfer and remote sensing," in *Remote Sensing of Coastal Aquatic Waters*, R. Miller and C. E. Del-Castillo, eds. (Springer/Kluwer, 2005), pp. 1–20.
53. S. Hooker, G. Zibordi, G. Lazin, and S. McLean, *The SeaBOARR-98 Field Campaign* (NASA Goddard Space Flight Center, 1999).
54. J. H. Morrow, S. Hooker, C. R. Booth, and J. W. Brown, *Advances in Measuring the Apparent Optical Properties (AOPs) of Optically Complex Waters* (NASA Goddard Space Flight Center, 2010).
55. R. C. Smith and K. S. Baker, "The analysis of ocean optical data," Proc. SPIE **0489**, 119–126 (1984).
56. R. C. Smith and K. S. Baker, "The analysis of ocean optical data II," Proc. SPIE **0637**, 95–107 (1986).
57. R. M. Pope and E. S. Fry, "Absorption spectrum (380–700 nm) of pure water.II. Integrating cavity measurements," Appl. Opt. **36**, 8710–8723 (1997).
58. J. R. V. Zaneveld, A. H. Barnard, and E. Boss, "Theoretical derivation of the depth average of remotely sensed optical parameters," Opt. Express **13**, 9052–9061 (2005).
59. C. D. Mobley, personal communication (2016).
60. C. D. Mobley and L. K. Sundman, *HYDROLIGHT 5.2 ECOLIGHT 5.2 Technical Documentation* (Sequoia Scientific, 2015).
61. G. R. Fournier and M. Jonasz, "Computer-based underwater imaging analysis," Proc. SPIE **3761**, 62–70 (1999).
62. M. Jonasz and G. R. Fournier, *Light Scattering by Particles in Water: Theoretical and Experimental Foundations*, 1st ed. (Elsevier, 2007).
63. H. R. Gordon, "The sensitivity of radiative transfer to small-angle scattering in the ocean: a quantitative assessment," Appl. Opt. **32**, 7505–7511 (1993).
64. T. Chai and R. R. Draxler, "Root mean square error (RMSE) or mean absolute error (MAE)?–arguments against avoiding RMSE in the literature," Geosci. Model Dev. **7**, 1247–1250 (2014).
65. E. Boss, W. H. Slade, M. Behrenfeld, and G. Dall'Olmo, "Acceptance angle effects on the beam attenuation in the ocean," Opt. Express **17**, 1535–1550 (2009).
66. Marcos, J. R. Seymour, M. Luhar, W. M. Durham, J. G. Mitchell, A. Macke, and R. Stocker, "Microbial alignment in flow changes ocean light climate," Proc. Natl. Acad. Sci. USA **108**, 3860–3864 (2011).
67. S. Talapatra, A. R. Nayak, C. Zhang, J. Hong, J. Katz, M. Twardowski, and A. P. D. J. Sullivan, "Characterization of organisms, particles, and bubbles in the water column using a free-drifting, submersible, digital holography system," in *Proceedings of 20th Ocean Optics Conference*, 27 September 2010.
68. J. R. V. Zaneveld and S. Pegau, "A model for the reflectance of thin layers, fronts, and internal waves and its inversion," Oceanography **11**, 44–47 (1998).
69. P.-W. Zhai, Y. Hu, C. R. Trepte, and P. L. Lucker, "A vector radiative transfer model for coupled atmosphere and ocean systems based on successive order of scattering method," Opt. Express **17**, 2057–2079 (2009).